STRUCTURE OF THE X-RAY–EMITTING GAS IN THE HYDRA A CLUSTER OF GALAXIES

Y. IKEBE,[1] K. MAKISHIMA,[2] H. EZAWA,[2] Y. FUKAZAWA,[2] M. HIRAYAMA,[2,3] H. HONDA,[3]
Y. ISHISAKI,[2,4] K. KIKUCHI,[4] H. KUBO,[2,3] T. MURAKAMI,[3] T. OHASHI,[4]
T. TAKAHASHI,[3] AND K. YAMASHITA[5]

ABSTRACT

The temperature and abundance structure in the intracluster medium (ICM) of the Hydra A Cluster of galaxies is studied with *ASCA* and *ROSAT*. The effect of the large extended outskirts in the point-spread function of the X-ray telescope on *ASCA* is included in this analysis. In the X-ray brightness profile, the strong central excess above a single β model, identified in the *Einstein* and *ROSAT* data, is also found in the harder energy band (>4 keV). A simultaneous fit of five annular spectra taken with the GIS instrument shows a radial distribution of the temperature and metal abundance. A significant central enhancement in the abundance distribution is found, while the temperature profile suggests that the ICM is approximately isothermal, with a temperature of ~ 3.5 keV. The *ROSAT* position-sensitive proportional counter (PSPC) spectrum in the central 1′.5 region indicates a significantly lower temperature than the GIS result. A joint analysis of the GIS and PSPC data reveals that the spectra can be described by a two-temperature model as well as by a cooling flow model. In both cases, the hot-phase gas with a temperature of ~ 3.5 keV occupies more than 90% of the total emission measure within 1′.5 from the cluster center. The estimated mass of the cooler (0.5–0.7 keV) component is $\sim (2-6) \times 10^9 \, M_\odot$, which is comparable to the mass of hot halos seen in non-cD ellipticals. The cooling flow model gives the mass deposition rate of $60 \pm 30 \, M_\odot \, \mathrm{yr}^{-1}$, an order of magnitude lower than the previous estimation.

Subject headings: galaxies: clusters: individual (Hydra A) — intergalactic medium — X-rays: galaxies

1. INTRODUCTION

X-ray imaging studies with the *Einstein Observatory* and *ROSAT* revealed that many clusters exhibit central concentrations in their X-ray brightness profiles. The central excess emission is often interpreted as a result of a cooling flow, a thermal instability occurring at the densest part of the cluster (see Fabian 1994 for a review). Edge, Stewart, & Fabian (1992) reported that about two-thirds of all known clusters have such structure, suggesting that this structure is a fairly common characteristic among clusters. Spectroscopic studies with *Einstein* and *ROSAT* found that there are cooler gas components with temperature $\sim 10^7$ K in cluster centers (e.g., Canizares et al. 1979). However, the previous spectroscopy is limited to the soft X-ray band ($\sim 0.1-4$ keV). *ASCA* has provided the first opportunity to resolve X-ray spectra spatially in the wider 0.5–10 keV energy range.

In this paper we report the *ASCA* observation of the Hydra A Cluster of galaxies ($z = 0.0522$). Its X-ray luminosity measured with the *Einstein Observatory* was

4.1×10^{44} ergs s^{-1} (0.5–4.5 keV) (David et al. 1990), and a consistent value of 4.8×10^{44} ergs s^{-1} in the same energy band was indicated from the *Ginga* observation that measured the X-ray spectrum in the 2–10 keV band (Tsuru 1991). These luminosities are among the largest of poor clusters (Kriss, Cioffi, & Canizares 1983; Tsuru 1991). The average X-ray temperature of ~ 4 keV, as measured with *Ginga*, is also rather high for a poor cluster.

The central region of this cluster is of particular interest. The cD galaxy 3C 218 = Hydra A is a strong radio source, with a very complex radio morphology and the highest Faraday rotation ever measured from a radio galaxy (Ekers & Simkin 1983; Kato et al. 1987; Taylor et al. 1990). Furthermore, the X-ray surface brightness profile obtained with the *Einstein* imaging proportional counter (IPC) exhibits a large central excess deviating from an isothermal β model, suggesting the presence of a cooling flow with an estimated mass deposition rate of $600 \pm 120 \, M_\odot \, \mathrm{yr}^{-1}$ (David et al. 1990). This is one of the largest values thus far attributed to the X-ray–emitting gas in clusters of galaxies (Edge et al. 1992).

When we analyze the *ASCA* data, the complex response of the X-Ray Telescope (XRT; Serlemitsos et al. 1995) on board *ASCA* introduces considerable difficulty for spatially resolved spectroscopy. To confront these difficulties, some analysis methods have been proposed (Ikebe 1995; Markevitch et al. 1996a; Churazor et al. 1996). The method employed in this paper is based on the similar idea in Markevitch et al. (1996a) but is performed with different implementation. Since the position resolution of *ASCA* is relatively poor, the sharp *ROSAT* image is also very helpful in analyzing the *ASCA* data. Assisted by the *ROSAT* image, we measured the spatial distribution of the temperature and metal abundance in the Hydra A Cluster from the *ASCA*

[1] Cosmic Radiation Laboratory, Institute of Physical and Chemical Research (RIKEN), 2-1 Hirosawa, Wako-shi, Saitama 351-01, Japan; ikebe@postman.riken.go.jp.

[2] Department of Physics, University of Tokyo, 3-1, Hongo 7-chome, Bunkyo-ku, Tokyo 113, Japan; maxima@miranda.phys.s.u-tokyo.ac.jp, ezawa@tkyosf1.phys.s.u-tokyo.ac.jp, fukazawa@miranda.phys.s.u-tokyo.ac.jp, hirayama@tkyosf1.phys.s.u-tokyo.ac.jp, hkubo@miranda.phys.s.u-tokyo.ac.jp.

[3] Institute of Space and Astronautical Science, 1-1, Yoshinodai 3-chome, Sagamihara-shi, Kanagawa 229, Japan; honda@astro.isas.ac.jp, murakami@astro.isas.ac.jp, takahasi@tkynext.astro.isas.ac.jp.

[4] Department of Physics, Tokyo Metropolitan University, 1-1, Minami-ooosawa, Hachioji-shi, Tokyo 192-03, Japan; ishisaki@phys.metro-u.ac.jp, kikuchi@phys.metro-u.ac.jp, ohashi@phys.metro-u.ac.jp.

[5] Department of Physics, Nagoya University, Furoucho, Chikusa-ku, Nagoya-shi, Aichi 464-01, Japan; yamasita@satio.phys.nagoya-u.ac.jp.

observation. In § 2 we describe the *ASCA* observation and the data selection procedure. Section 3 gives the results using a conventional analysis method on the GIS and SIS data. Section 4 describes the analysis method developed here. In § 5 we analyze the X-ray brightness profiles in different energy bands. In § 6 we describe the temperature and abundance structure studied using the GIS spectra, and we also discuss the joint analysis of the *ROSAT* and *ASCA* data to study the temperature structure in the central region. We discuss the results and summarize them in § 7. $H_0 = 50$ km s^{-1} Mpc^{-1} is assumed throughout.

2. *ASCA* OBSERVATION AND DATA SELECTION

ASCA (Tanaka, Inoue, & Holt 1994) observed the Hydra A Cluster during the performance verification phase on 1993 May 28 and 29. The two GIS detectors (Ohashi et al. 1996; Makishima et al. 1996), GIS-S2 and GIS-S3, were operated in pulse height normal mode. The two SIS sensors, SIS-S0 and SIS-S1, were operated in 4 CCD faint or bright mode, and the central region of the Hydra A Cluster was detected in the middle of chip 1 and chip 2 of SIS-S0, and chip 3 and chip 0 of SIS-S1.

We have applied the standard data cleaning procedure (see Day et al. 1995) to the GIS and SIS data, and selected the data with the criteria that the cutoff rigidity and elevation angle must be greater than 8 GeV/c and 5°.0, respectively. The additional selection criterion that the elevation angle from the sunlit Earth is greater than 20° was applied to the SIS data only. In the present analysis, 24.4 ks of the SIS-S0 data, 22.7 ks of the SIS-S1 data, and 26.3 ks of the GIS data survived these selection criteria. The X-ray intensity contour map from the summed GIS-S2 and S3 data is shown in Figure 1. As the background (cosmic X-ray background plus non–X-ray background) of the GIS data, we utilized the data from the *Lynx field*, which was observed on 1993 May 13–15 when the spread discriminator in the on-

board CPU of GIS was disabled as it was for the Hydra A Cluster (see Makishima et al. 1996). For the SIS background we used the data of several blank sky fields observed during the performance verification phase.

3. ANNULAR SPECTRAL ANALYSIS

For detailed study of the spatial variations in the spectra, energy spectra are often accumulated from different regions and are analyzed individually (see, e.g., Ohashi et al. 1994; Ikebe et al. 1994). However, this conventional analysis method is no longer usable for the *ASCA* data on clusters of galaxies. Although the *ASCA* XRT has a sharply peaked point-spread function (PSF) with about 3' half-power diameter (HPD), the PSF has wide outskirts with significant flux extending over the whole GIS field of view of 52' diameter (Serlemitsos et al. 1995). Therefore, individual regions on the focal plane have inevitable contributions of the flux from other regions. Moreover, such a flux-mixing effect depends considerably on the X-ray energy because the PSF has wider outskirts at higher energies. In particular, this energy-dependent flux-mixing effect is quite serious for the study of clusters of galaxies. Since their X-ray surface brightness decreases from center to periphery by several orders of magnitude, the outer regions of clusters inevitably have a considerable and energy-dependent flux from the inner, much brighter parts. Therefore, the meaning of the individual spectra accumulated over specified areas in the focal plane is very unclear. Figure 2 demonstrates the mutual contribution of X-ray flux from annular sky regions to the annular regions on the focal plane in the case of the Hydra A Cluster.

Although the results are not accurate, in this section we first perform model fittings to individual annular spectra, as has been done in previous papers on the *ASCA* data. This is to illustrate the results when the energy-dependent flux-mixing effect is not considered, and to compare them with the results from the analysis method described in the subsequent sections.
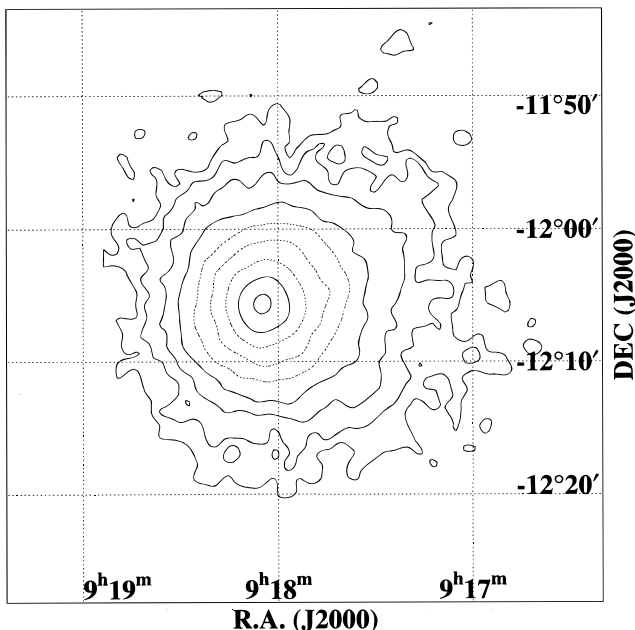

FIG. 1.—X-ray intensity contour map of the Hydra-A cluster obtained with the GIS. The background-subtracted image was convolved with a Gaussian of 1' FWHM. The contours are logarithmic, where each step corresponds to a multiplicative factor of 2.
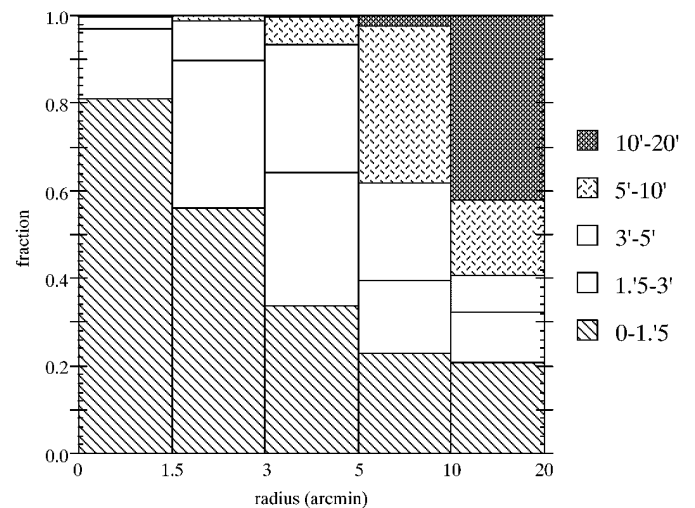

FIG. 2.—X-ray flux contributions from the sky annular regions to the individual annular spectra of the GIS are illustrated. We simulated the GIS data of an isothermal symmetric cluster having the radial brightness profile shown in Fig. 8. The temperature, heavy-element abundance, and hydrogen column density are assumed to be 4 keV, 0.3 solar, and 5×10^{20} cm^{-2}, respectively. On the horizontal axis the radius ranges of extracted spectra on the detector are plotted. The vertical axis shows the contribution fraction from different sky regions, illustrated with different patterns.
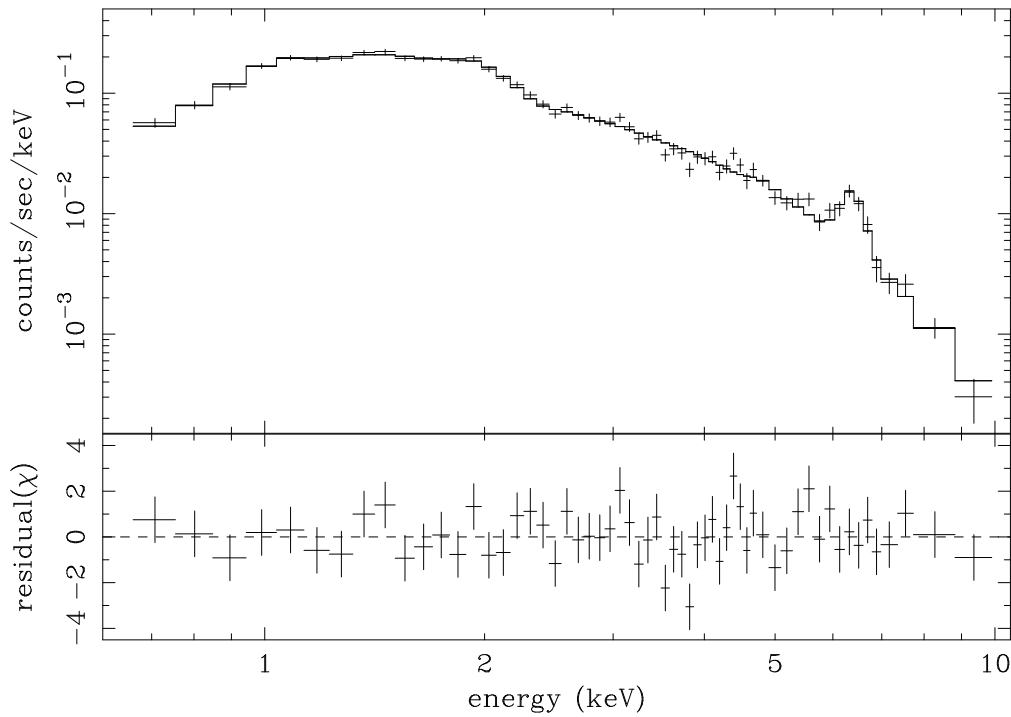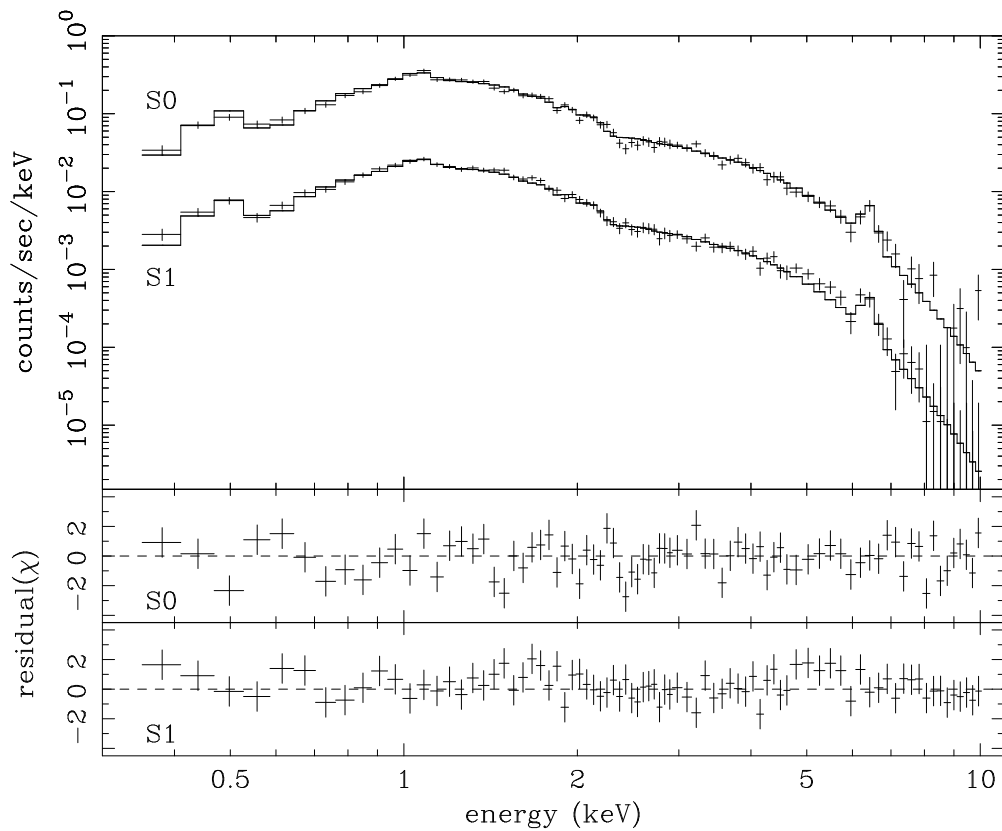
Fig. 3.—(a) GIS and (b) SIS spectra extracted from the central 1′.5 radius region fitted with a thermal bremsstrahlung plus three emission lines modified by the photoelectric absorption. Crosses represent the data, and histograms the model. For the display, SIS-S1 data and its model are multiplied by 0.1.

The GIS and SIS spectra have been accumulated in concentric annular regions centered on the cD galaxy, covering radius ranges of 0′–1′.5, 1′.5–3′, 3′–5′, 5′–10′, and 10′–20′. The data of GIS-S2 and GIS-S3 were then combined after the correction for the gain difference. For the SIS, data from four different chips in the same detector were combined after relative gain corrections. The SIS and GIS spectra thus obtained both exhibit strong emission lines from highly
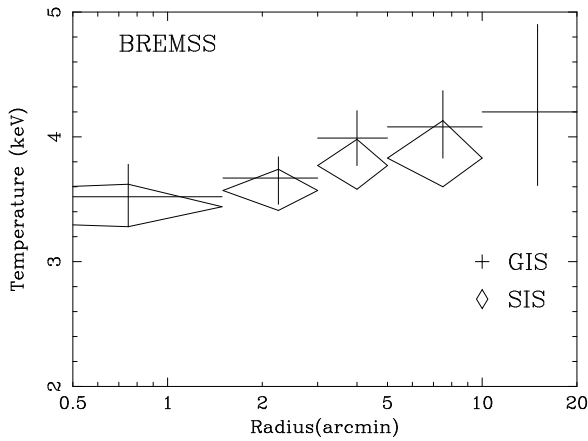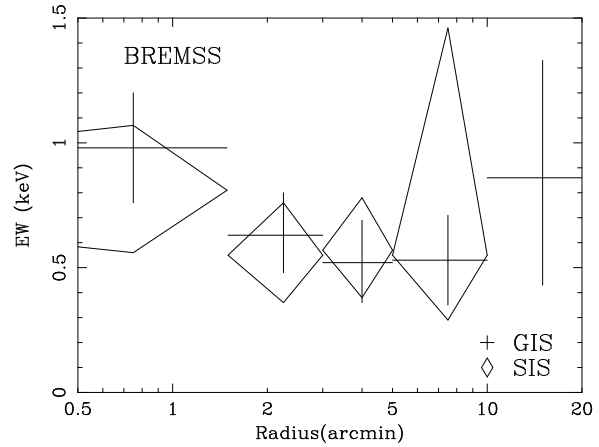
FIG. 4a

FIG. 4b

FIG. 4.— Results of the annular spectral fits with a thermal bremsstrahlung plus three emission lines: (a) temperature and (b) equivalent width of Fe K lines are illustrated.

ionized ions. We fitted annular spectra individually with a thermal bremsstrahlung model plus Gaussians modified by photoelectric absorption, using the XSPEC package (Version 9.0). The energy ranges used for the fitting are 0.7–10 keV and 0.35–10 keV for the GIS and SIS, respectively. For all the spectral fittings, we used the XRT effective area, which is calculated assuming that the point source is being observed with a circular detector of 6′ radius size. Figure 3 shows the central 0′–1′.5 spectra together with the best-fit model. At least three Gaussians at the rest-frame energies of 6.7 keV, ∼2.0 keV and ∼1.0 keV are required, which may correspond to the He-like Fe Kα, He- and H-like Si Kα, and a mixture of He-like Fe Lα and H-like Ne Kα emission lines, respectively. There is also some indication of a line structure at ∼1.5 keV, which may consist of He-like Fe Lβ and H-like Mg Kα emission lines. The continuum is well described by a single-temperature model. When we performed the fitting using only the less than 3 keV energy band or the greater than 3 keV energy band, the best-fit temperatures were not different. The two-temperature model did not improve the best-fit χ^2 values at all. We illustrate the projected radial profiles of the temperature and the equivalent width (EW) of the Fe K emission lines in Figure 4. Unless otherwise specified, all errors

are 90% confidence for one parameter of interest ($\Delta\chi^2 = 2.71$). The two instruments have given consistent results, and the gradual increase toward the outside is seen in the temperature profile.

We also fitted the spectra with the single-temperature thin thermal plasma emission model by Raymond & Smith (1977, hereafter "the RS model"). The temperature, heavy-element abundances, and normalization were varied as free parameters, while relative abundance ratios were fixed at the solar values given by Anders & Grevesse (1989). The projected radial profiles of temperature and abundance derived are shown in Figure 5. The temperature profile obtained exhibits a gradual increase toward the outside and is consistent with the result from the fits with a thermal bremsstrahlung model plus Gaussians (Fig. 4a). The abundance values obtained with the SIS are significantly smaller than those obtained with the GIS (Fig. 5b). The same systematic difference has been found in the data from various clusters observed with *ASCA* (Fukazawa 1996). This may be because the actual SIS energy resolution is slightly worse than the prediction of the response matrix, probably because of the chip summation. When we applied an alternative plasma emission model, the Mewe-Kaastra model (hereafter "the MEKA model"; Mewe, Gronenschild, &
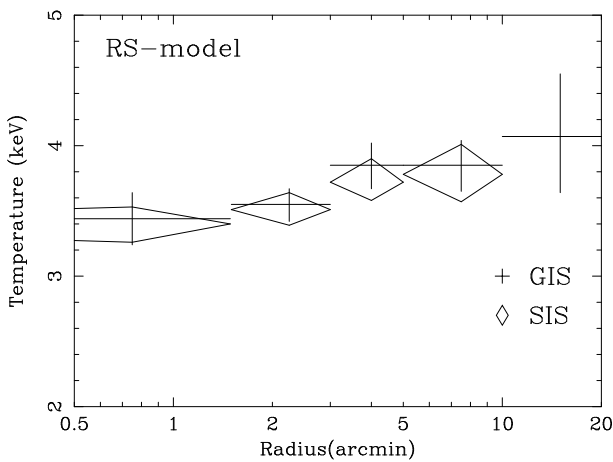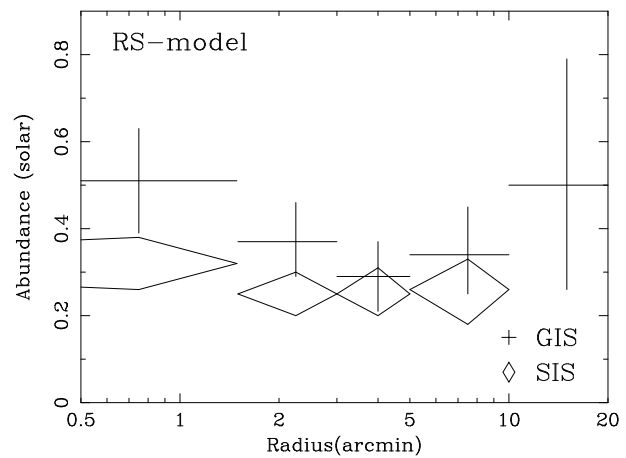

FIG. 5a

FIG. 5b

FIG. 5.—Results of the annular spectral fits with RS model: (a) temperature and (b) abundance are illustrated

van den Oord 1985; Mewe, Lemen, & van den Oord 1986; Kaastra 1992), we derived results consistent with those from the RS model. Consistency between RS model and MEKA model results has been found from the *ASCA* data of other clusters with temperatures of ~ 3–4 keV (Mushotzky et al. 1996). As already pointed out, we cannot interpret the radial profiles presented in Figures 4 and 5 as true projected structure on the sky. The gradual increase toward the outside seen in the temperature profiles is not a real temperature structure but is likely to be an artifact due to the XRT responses. Simulations assuming an isothermal distribution also produce a similar temperature profile (Takahashi et al. 1995).

4. ANALYSIS METHOD FOR THE EXTENDED SOURCES

4.1. *Analysis Methods*

One way to analyze extended sources is to perform simultaneous fitting of the X-ray image and the spectra; that is, simultaneous fitting of the spectra extracted from different regions or, similarly, simultaneous fitting of the images sorted in different energy bands. We start with an X-ray source model which, in the case of a cluster, describes spatial distributions of the X-ray emissivity, temperature, and abundance. A given model is converted to the simulated *ASCA* data through the convolution calculations with the instrument responses, which include the XRT PSF and effective area as well as the quantum efficiency and energy redistribution function of the GIS or SIS. The goodness of fit of the model is evaluated by comparing the simulated data with the observed data, and the results are iteratively fed back to the input model.

The XRT + GIS PSFs used in our analysis were produced by interpolating the X-ray images of Cyg X-1 actually obtained with GIS. However, Cyg X-1 is so bright that the SIS cannot measure its brightness profile precisely because of event pileup, and thus cannot reproduce the XRT+SIS PSFs with the same method. Therefore, in this paper we analyzed only the GIS data with the analysis method described here. The detailed description of PSF calibration is given in the Appendix.

A technical problem in this analysis is how to reduce the calculation time. The image convolution, which is the most time-consuming part, is mathematically expressed as an operation by the two-dimensional matrix called the *image response matrix* with size as large as $\sim 20,000 \times 20,000$ for the GIS full-resolution image. To reduce the calculation time, we have developed an analysis method using the Monte Carlo technique (Takahashi et al. 1995; Ikebe 1995), which is often much faster than the huge matrix operation. We only need to generate events more numerous, say by a factor of 10, than the actual events. This Monte Carlo method was employed for the analysis of the Fornax Cluster (Ikebe et al. 1996); the Centaurus Cluster (Ikebe 1995); 3A 0336+098, A1795, MKW 3s, and PKS 2354−35 (Ohashi et al. 1995; Kikuchi et al. 1995); the Ophiuchus Cluster (Matsuzawa et al. 1996); and the Coma Cluster (Honda et al. 1996).

4.2. *Image Response Matrices*

An alternative method for reducing the calculation time is to reduce the size of the image response matrix. Owing to the limited number of observed photons, we usually bin the image so that each image pixel has a sufficient number of

events that χ^2 statistics can be employed. Moreover, an X-ray source model given is often so simple that the number of sky regions can be largely reduced. Thus, the dimension of the image response matrix can be reduced drastically.

Since the Hydra A Cluster can be reasonably modeled with a circularly symmetrical model, as will be described in the following sections, we employed the matrix operation to generate simulated data rather than using the Monte Carlo method. This method was first proposed by Markevitch et al. (1996a) and had been applied to the *ASCA* data analysis of A2163, A754, A2256, A2319, A665, Triangulum Australis, A3558, and AWM 7. (Markevitch et al. 1996a; Henriksen & Markevitch 1996; Markevitch 1996; Markevitch, Sarazin, & Irwin 1996b; Markevitch & Vikhlinin 1997). Here we recall the formula of the matrix operation and define the χ^2 function for the minimum χ^2 fitting.

The model prediction is given by the form

$$\mathrm{MODEL}_{\mathrm{pi}}^{\mathrm{det}} = \sum_{\mathrm{energy}} \sum_{\mathrm{sky}} \mathrm{RMF}_{\mathrm{pi, energy}} \, \mathrm{IRM}_{\mathrm{energy}}^{\mathrm{det, sky}} S_{\mathrm{energy}}^{\mathrm{sky}} , \quad (1)$$

where IRM is the image response matrix, which is defined as

$$\mathrm{IRM}_{\mathrm{energy}}^{\mathrm{det, sky}} = \mathrm{PSF}_{\mathrm{energy}}^{\mathrm{det, sky}} \mathrm{EFF}_{\mathrm{energy}}^{\mathrm{sky}} . \quad (2)$$

Here S is the initial cluster model on the sky which gives the X-ray surface brightness as a function of X-ray energy (expressed with the subscript "energy") and sky position ("sky"); EFF is the effective area including quantum efficiency of the focal-plane instruments expressed as a function of X-ray energy and sky position; PSF is the XRT PSF which gives the photon distribution on the detector ("det") depending on the X-ray energy and sky position; and RMF is the energy redistribution function which expresses pulse-height–invariant ("pi") distribution for an incident monochromatic-energy X-ray event. While both the *ASCA* data and the initial cluster model on the sky (S) have three dimensions, the fitting is performed in the form of some energy-sorted brightness profiles, or in the form of some ring-sorted spectra.

To evaluate the best-fit parameters of the assumed model, we defined the χ^2 function as

$$\chi^2 = \sum_{\mathrm{det}} \sum_{\mathrm{pi}} \frac{(\mathrm{DATA}_{\mathrm{pi}}^{\mathrm{det}} - \mathrm{BGD}_{\mathrm{pi}}^{\mathrm{det}} - \mathrm{MODEL}_{\mathrm{pi}}^{\mathrm{det}})^2}{(\sigma_{\mathrm{pi}}^{\mathrm{det}})^2} , \quad (3)$$

where

$$(\sigma_{\mathrm{pi}}^{\mathrm{det}})^2 = \sigma_{\mathrm{DATA}_{\mathrm{pi}^{\mathrm{det}}}}^2 + \sigma_{\mathrm{BGD}_{\mathrm{pi}^{\mathrm{det}}}}^2 + (a \times \mathrm{BGD}_{\mathrm{pi}}^{\mathrm{det}})^2$$
$$+ (b \times \mathrm{MODEL}_{\mathrm{pi}}^{\mathrm{det}})^2 . \quad (4)$$

Here DATA, BGD, and MODEL are the values of the observed data counts, the normalized background, and the model, respectively. $\sigma_{\mathrm{DATA}_{\mathrm{pi}^{\mathrm{det}}}}$ and $\sigma_{\mathrm{BGD}_{\mathrm{pi}^{\mathrm{det}}}}$ are statistical errors associated with respective quantities, while the latter two terms in equation (4) represent systematic errors. The systematic error of the image response matrix is included in the χ^2 value by adding 5% ($b = 0.05$) of the model flux. We also introduced 10% of the background intensity estimated from the blank-sky data in the systematic errors; that is, $a = 0.1$.

We have checked the consistency between the Monte Carlo method and results from the image response matrices. For example, from a best-fit model obtained by fitting using the image response matrices, the Monte Carlo simulation can reproduce the data that agree with the actual data with sufficient accuracy.

5. RADIAL BRIGHTNESS PROFILE

5.1. ASCA Data and Fitting Results

Using the analysis method described in § 4.2, we first analyzed the X-ray images taken with the GIS. The X-ray image has a good circular symmetry, and the azimuthally averaged background-subtracted radial brightness profiles in different energy ranges are shown in Figure 6. They are centered on the peak of the X-ray intensity and have 20 bins in total of 1′ width each. With ASCA we were able to obtain the image in the 4–10 keV range for the first time, and these radial profiles are very similar among different energy bands.

In order to perform the model fitting to the radial profile following the method described in § 4.2, we constructed image response matrices of size 26×20 for each of the 201 energy bins. Each matrix represents flux contribution from 26 sky regions to the 20 regions on the focal plane at a specified energy. The 26 sky regions employed here are 8 annular regions of 0′.25 width for $r < 2'$ and 18 annular regions of 1′ width for $r = 2'$–$20'$, while the detector region was divided into 20 annular bins of 1′ width each. Since the matrix used for the fitting represents contributions only from sky regions within 20′ radius, it is implicitly assumed that no emission is generated outside the 20′ radius. This assumption is consistent with the ROSAT image, which will be described in the next section, and even when we assume the maximum radius to be larger than 20′, the fitting results do not change significantly.

As the model brightness profile, we employed an empirical β model expressed as

$$\Sigma(r) = \Sigma_0 \left[1 + \left(\frac{r}{r_c} \right)^2 \right]^{-3\beta + 0.5}, \qquad (5)$$

where r is the projected angular distance from the center, β represents the beta parameter, and r_c is the core radius. We assume that the energy spectrum takes the same form in the entire cluster and is expressed with the RS model modified by the Galactic absorption. The temperature, heavy-element abundance, and hydrogen column density are assumed to be 3.4 keV, 0.5 solar, and 6×10^{20} cm^{-2}, respectively, as derived in § 3 from the spectral fitting of the GIS data extracted from the innermost region. The free parameters are r_c, β, and Σ_0.
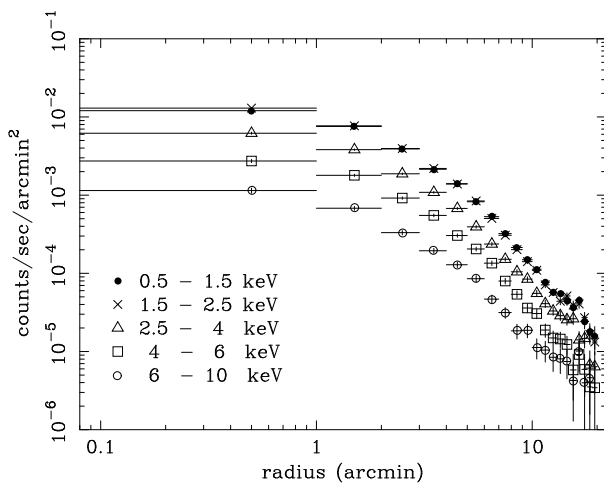

FIG. 6.—Background-subtracted radial brightness profiles in different energy ranges obtained by the GIS.

Energy Range (keV)	r_c (arcmin)	β	χ^2/ν
0.5–1.5	0.97 (0.71–1.25)	0.62 (0.58–0.66)	10.5/17
1.5–2.5	0.96 (0.70–1.30)	0.63 (0.59–0.68)	15.1/17
2.5–4	1.14 (0.69–1.35)	0.67 (0.58–0.68)	7.0/17
4–6	1.54 (1.10–2.25)	0.72 (0.64–0.87)	5.6/17
6–10	1.20 (0.58–2.05)	0.67 (0.56–0.87)	7.3/17

NOTE.—Errors represent the 90% confidence limit for two parameters of interest.

With this single β model, we fitted the individual radial profiles in Figure 6 and obtained acceptable fits for all energy bands. The best-fit parameters are summarized in Table 1. We can compare this with the results from the Einstein IPC; that is, the detection of the central excess emission above a β model (David et al. 1990). Since ASCA has a much poorer angular resolution than the Einstein IPC, the central excess in the IPC data may be unresolved in the ASCA data. Thus we obtain a single β model with core radius smaller than 1′.6, consistent with the results obtained from IPC data in the $r > 1'.5$ region (David et al. 1990). In fact, the GIS radial profiles are well reproduced by convolving the ROSAT PSPC image with the ASCA response (see § 5.3). The important result here is that all the radial brightness profiles in different energy bands show an almost identical shape, as can be seen from Table 1. This suggests that the central excess emission may be present in higher energy bands as well as in the soft energy band. We will come back to this issue later.

5.2. ROSAT Data and Analysis

As described in § 4, to obtain the temperature structure in the Hydra A Cluster, we need to fit the X-ray image and spectra simultaneously. However, the brightness profile obtained from the GIS data alone would be highly model dependent because of the relatively wide PSFs. An alternative, preferable way is to utilize the ROSAT image itself as the model of the brightness profile, as has been done in Markevitch et al. (1996a). We thus analyzed the data of the ROSAT PSPC.

The ROSAT PSPC observed the Hydra A Cluster from 1992 November 8 to 1992 November 9 with a total on-target exposure time of 18 ks and the pointing position of 9^{h}18^{m}05^s, $-12°06'00''$ (J2000). We obtained the processed data of the PSPC from the archival database provided by the ROSAT Guest Observer Facility at the NASA/Goddard Space Flight Center. For the data reduction we followed the procedure described by Snowden et al. (1994) and used their software (Snowden 1995).

From the PSPC data, the valid time is selected so that the Master Veto count rate is always smaller than 170 counts s^{-1} to eliminate the data with anomalously high particle background rates (Snowden et al. 1992; Plucinsky et al. 1993). Using Snowden's software, we can estimate the count rate of the four background components, the particle background (PB), afterpulse events (APs), scattered solar X-ray background (SB), and long-term enhancements (LTEs). After subtracting the background, the PSPC image was corrected using the exposure map, which represents the effective area and the exposure time as a function of the position in the sky coordinates. We thus obtained the back-
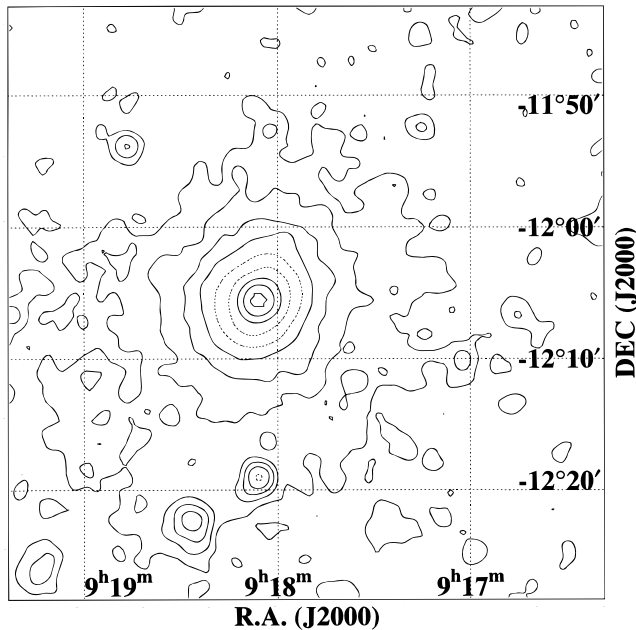
FIG. 7.—X-ray intensity contour map obtained with the *ROSAT* PSPC. The image was smoothed with a Gaussian of 1′ FWHM. The contours are logarithmic, where each step corresponds to a multiplicative factor of 2.

ground-subtracted flat-field images in the 0.14–2.04 keV band (Fig. 7). In the PSPC data, X-ray flux from the cluster is detected out to ∼20′.

The X-ray image taken by the PSPC exhibits very good circular symmetry. To express the X-ray brightness profile quantitatively, we performed model fitting to the radial brightness profiles. We assumed that the PSPC point-source responses are ideally pointlike; this is true if we are not discussing structures smaller than ∼1′. First, we fitted the PSPC radial profile with a single-β model, but the fit was quite poor. As a next step, we applied a sum of two β models to fit the profile and derived a good fit as shown in Figure 8. The best-fit parameters of the two β models are $(r_c, \beta) = (1\rlap{.}'36, 2.5)$ for the narrower component, and $(r_c, \beta) = (1\rlap{.}'80, 0.68)$ for the wider component. In the narrower component the intensity is reduced by half at $r = 0\rlap{.}'44$. The normalization ratio of the two β models, $f \equiv$ (normalization
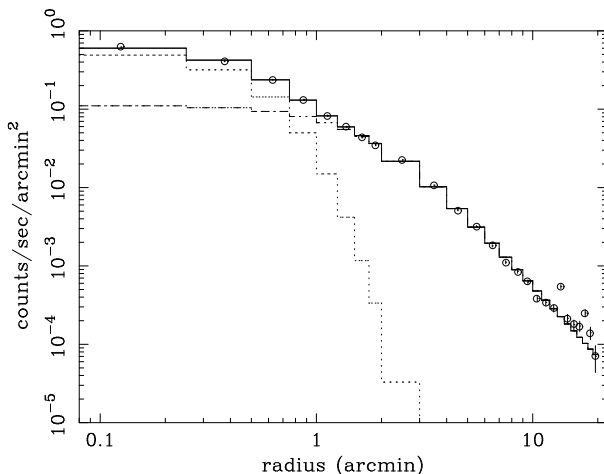

FIG. 8.—Background-subtracted PSPC radial profile fitted with the double β model. Open circles represent the data, and histograms the models.
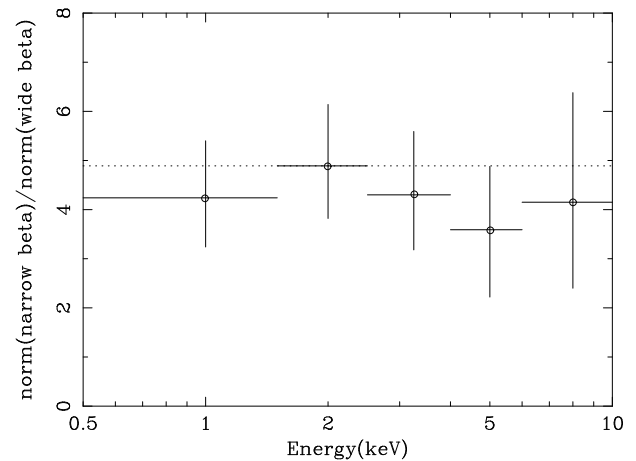

FIG. 9.—Best-fit normalization ratios between narrow β and wide β components. The errors represent the 90% confidence limit.

of the narrow β model)/(normalization of the wide β model), is 4.9. This reconfirms the existence of the central excess emission found with the *Einstein* IPC.

5.3. *Combined ASCA and ROSAT Data*

In the soft X-ray band where *ROSAT* and *ASCA* are both sensitive, the *ASCA* radial profile also must be fitted with the same double-β model that fitted the PSPC radial profile. Thus, we fitted the GIS radial profile in 0.5–2.5 keV with the double-β model, in which the two sets of β parameters and core radii (r_c), and the ratio between the two normalizations (f) were fixed at the best-fit values derived in § 5.2. We derived a good fit, and the obtained minimum χ^2 value was $20.5/(\nu = 19)$.

In the higher energy bands, does the radial profile require a central excess? In the previous section we suggested that the similar radial profiles in different energy bands could be evidence of the existence of the central excess emission in the higher energy bands as well. Using the double-β model, we have checked whether the higher energy bands also show the central excess or not. In this case we let the normalizations for the two β model components vary independently, while the two sets of β parameters and core radii were fixed to the values that were obtained in § 5.2. The fitting results are illustrated in Figure 9. In all energy ranges, the normalization ratios (f) obtained are consistent with 4.9, which is the best-fit value obtained with the PSPC radial profile in § 5.2. Moreover, when we fixed the normalization of the narrow β component to be zero, the fit became unacceptable; the minimum χ^2 values are 101, 133, 81, 48, and 30, with $\nu = 19$ for the 0.5–1.5 keV, 1.5–2.5 keV, 2.5–4 keV, 4–6 keV, and 6–10 keV ranges, respectively. These results imply that the narrower of the two β model components is definitely needed in individual radial profiles, not only in the soft X-ray band but also in the harder energy ranges. Therefore, we can conclude that the central excess emission is most likely to be present in the higher energy band above 4 keV as well as in the soft X-ray band.

6. TEMPERATURE AND ABUNDANCE STRUCTURE

6.1. *Temperature and Abundance Profile*

In the last section we studied the radial brightness profiles in different energy ranges. In this section we describe

TABLE 2

SIMULTANEOUS FITTING OF THE FIVE GIS ANNULAR SPECTRA

PARAMETER	RADIUS (arcmin)				
	0–1.5	1.5–3	3–5	5–10	10–20
Temperature (keV)......	$3.41^{+0.20}_{-0.25}$	$4.26^{+1.11}_{-0.81}$	$4.08^{+1.09}_{-1.18}$	$3.62^{+0.98}_{-0.60}$	$2.77^{+0.75}_{-0.60}$
Abundance (solar)	$0.57^{+0.25}_{-0.21}$	0.17 (<0.55)	0.015 (<0.74)	0.25 (<0.71)	0.25 (<0.94)

NOTE.—For all five regions N_H ($\times 10^{20}$cm^{-2}) = 1.7 (<3.9); χ^2/ν = 237.1/283. Errors represent the 90% confidence limit for one parameter of interest.

the temperature and abundance profile based on the spatially sorted energy spectra. Using the method described in § 4, we performed simultaneous fitting to the five GIS annular spectra that were fitted individually in § 3, fully accounting for the contributions of the X-ray flux from the sky to the focal plane. The image response matrices used for this analysis have the dimension of 26×5 for each of the 201 energy bins. Twenty-six model regions consist of 8 annuli each 0.25 wide for $r = 0'–2'$ and 18 annuli each 1' wide for $r = 2'–20'$.

As the model brightness profile, we employed the PSPC radial brightness profile obtained in § 5. We assumed that the PSPC image represents the surface brightness profile in the energy range below 2 keV, and converted those surface brightness to emission measures according to the plasma emission code for a given temperature and abundance. The projected profiles of the temperature and abundance were assumed to be constant within the individual five annular regions of 0'–1.5, 1.5–3', 3'–5', 5'–10', and 10'–20', which correspond to the same five annular regions used in extracting the GIS spectra in detector coordinates. The hydrogen column density is assumed to be constant over the entire cluster. Therefore, the free parameters are five temperatures, five abundances, the hydrogen column density, and the overall normalization.

The best-fit parameters are summarized in Table 2, and the temperature and abundance profiles are represented in Figure 10 by crosses. Except for the central region, there seems to be an indication of a gradual temperature decrease toward the outside, but it is not statistically significant. In the abundance distribution, only the central value was well constrained, while only upper limits were obtained for the outer regions. However, the central abundance value is larger than all other best-fit values in the outer regions. This

suggests that there is a central concentration in the abundance distribution. In order to see the difference between the central 1.5 region and the outside region more clearly, we again fitted the five GIS spectra simultaneously assuming a common temperature and abundance outside 1.5. The results are summarized in Table 3 and represented in Figure 10 by diamonds. The central 1.5 abundance value is significantly larger than that of the outside, implying that there is a central concentration in the abundance distribution.

6.2. Central Cool Region

Since the radiative cooling time in the central region of the Hydra A Cluster is shorter than the Hubble time (2×10^{10} yr), the presence of a cooling flow is expected as discussed by David et al. (1990). If there is no significant heat input, the thermal instability occurs in the central, densest part of the cluster gas, and a rapid radiative-cooling process would lead to the formation of a cooler gas phase surrounded by the hotter ICM. As presented in the previous sections, the *ASCA* spectral analysis showed that the X-ray emission from the central 1.5 radius region can be attrib-

TABLE 3

OBTAINED TEMPERATURES AND ABUNDANCES IN THE CENTRAL 1.5 REGION AND THE OUTSIDE REGION

PARAMETER	RADIUS (arcmin)	
	0–1.5	1.5–20
Temperature (keV)......	3.55 ± 0.18	$3.91^{+0.24}_{-0.23}$
Abundance (solar)	$0.56^{+0.18}_{-0.16}$	0.14 ± 0.11

NOTE.—For both regions N_H ($\times 10^{20}$ cm^{-2}) = 1.2 (<3.2); χ^2/ν = 247.3/289. Errors represent the 90% confidence limit for one parameter of interest.
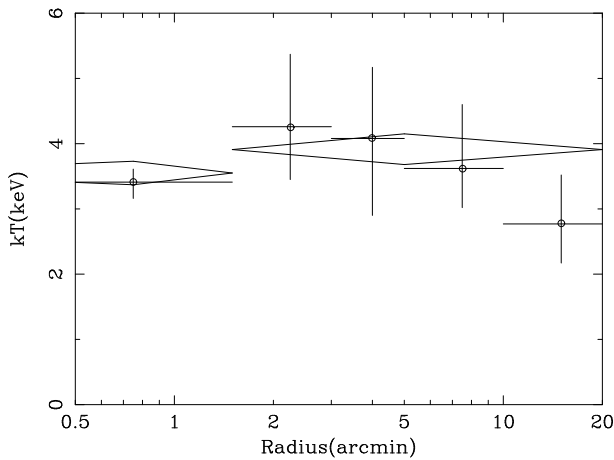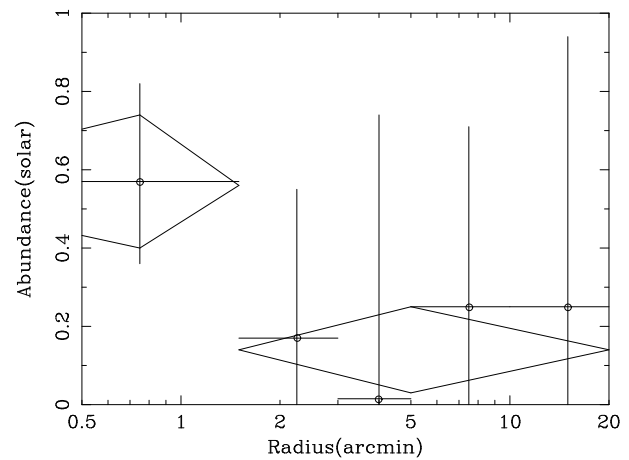

FIG. 10a

FIG. 10b

FIG. 10.—Radial profiles of (a) temperature and (b) abundance derived from the simultaneous fitting of the five GIS annular spectra.
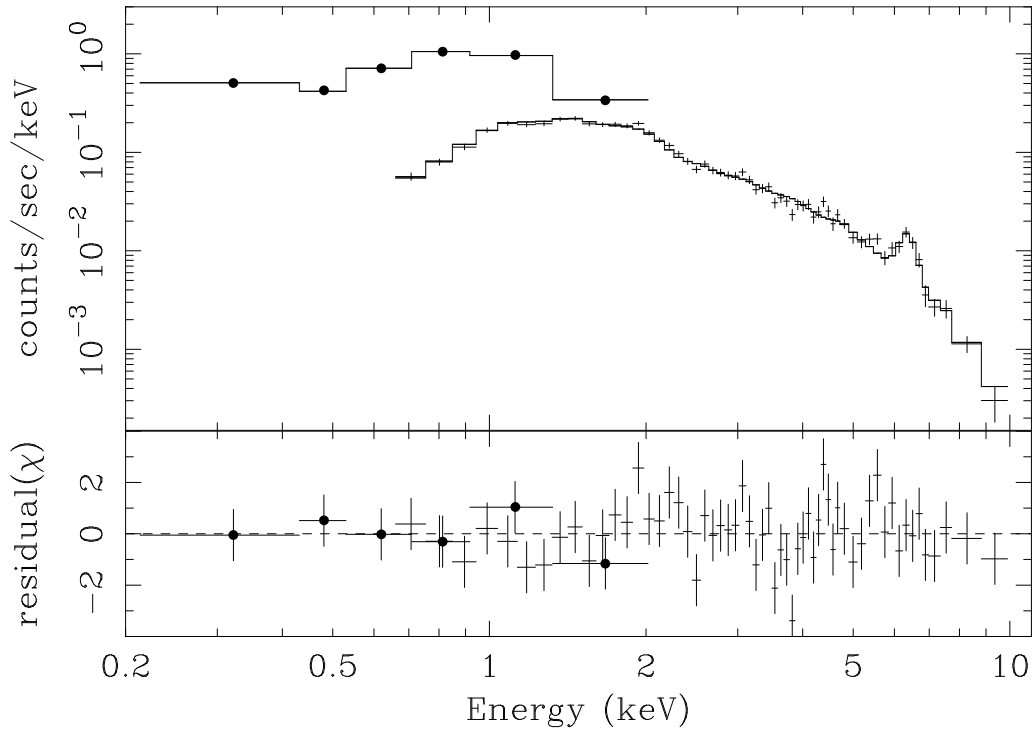
FIG. 11.—Simultaneous fitting of the PSPC and GIS spectra extracted from the central 1.5 radius region. Filled circles are for the PSPC data, and crosses for the GIS data. Histograms are for the best-fit two-temperature model.

uted to the 3.4 keV gas, and there is no clear evidence of a central cooler gas component. However, the GIS and SIS efficiencies decrease so rapidly below 1 keV that *ASCA* is not very sensitive to emission from gas cooler than ~ 1 keV. The *ROSAT* PSPC is sensitive down to ~ 0.1 keV, and thus these data would be useful to investigate whether there is an

additional central cooler gas component. In the following, we describe the results from the PSPC spectral fitting and joint analysis of the PSPC and GIS spectra.

We analyzed the *ROSAT* PSPC data first. From the same data set selected in § 5.2, we accumulated the pulse-height spectrum in the central 1.5 region. Each X-ray event

TABLE 4

SIMULTANEOUS FITTING OF THE PSPC AND GIS SPECTRA WITH A TWO-TEMPERATURE MODEL

Plasma Code	T_{cool} (keV)	T_{hot} (keV)	$EM(T_{cool})$ (cm^{-3})	$EM(T_{hot})$ (cm^{-3})	Abundance ($\times$ solar)	N_H (cm^{-2})	χ^2/ν
RS............	0.67	3.45	3.9×10^{65}	2.4×10^{67}	0.51	3.4×10^{20}	74.15/58
MEKA	0.50	3.41	4.1×10^{65}	2.4×10^{67}	0.56	3.4×10^{20}	73.97/58

NOTE.—Both the PSPC and the GIS spectra were extracted from the central 1.5 region. The fitting model is expressed with the sum of two RS models or MEKA models modified by photoelectric absorption.
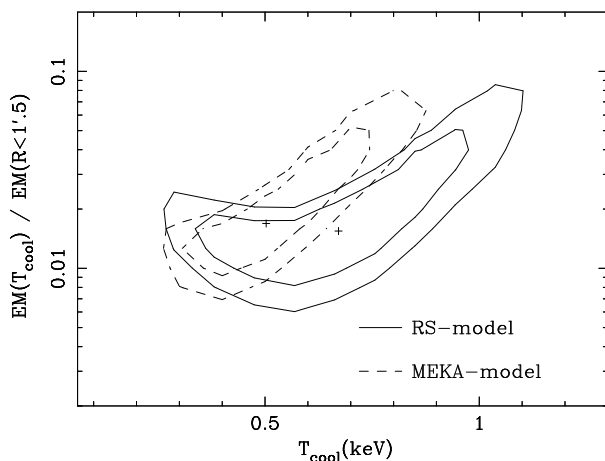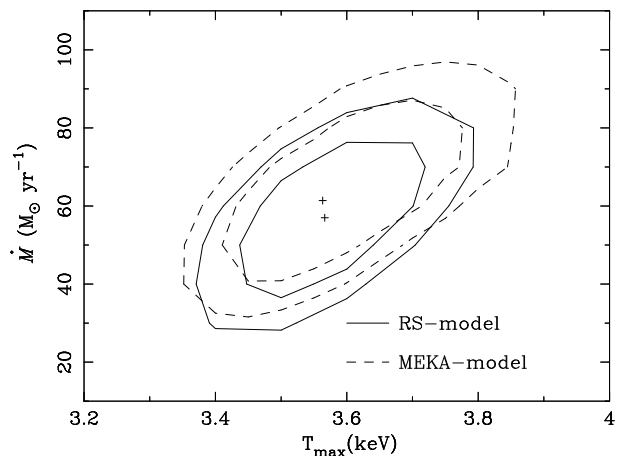

FIG. 12a

FIG. 12b

FIG. 12.—χ^2 contour map, (a) for the temperature of the cool component (T_{cool}) vs. fraction of the cool component (F_{cool}; see text) and (b) for the mass deposition rate ($\dot{M}$) vs. maximum temperature (T_{max}).

TABLE 5

SIMULTANEOUS FITTING OF THE PSPC AND GIS SPECTRA WITH A COOLING FLOW MODEL

Plasma Code	$\dot{M}$ ($M_\odot$ yr^{-1})	T_{hot} (keV)	EM(Cooling Flow) (cm^{-3})	EM(T_{hot}) (cm^{-3})	Abundance ($\times$ solar)	N_H (cm^{-2})	χ^2/ν
RS...........	57	3.57	2.0×10^{66}	2.3×10^{67}	0.50	3.3×10^{20}	73.85/59
MEKA	62	3.56	2.2×10^{66}	2.2×10^{67}	0.51	3.4×10^{20}	73.72/59

was weighted using the vignetting function so that the X-ray image became flat. The original 256 channel bins are summed up into seven energy bands named R1L–R7, defined in Snowden et al. (1994). For the model fitting we used only the six bins R2–R7 to avoid the afterpulse event contamination which could be contributing to the R1L band. The background spectrum was made from the annular region of $r = 36'-46'$, where no apparent point source was found.

We fitted the PSPC spectrum thus obtained with a single-temperature RS model as well as the MEKA model, with the response matrix named "pspcb_gain2_256.rsp" publicly available from NASA/Goddard Space Flight Center. The best-fit temperature, abundance, and hydrogen column density and their 90% confidence errors for one parameter of interest obtained with the RS model were 2.27 (2.03–2.63) keV, 0.30 (0.21–0.42) solar, and 3.79 (3.59–3.99) $\times 10^{20}$ cm^{-2}, respectively. The MEKA model gave 2.25 (2.00–2.55) keV, 0.33 (0.23–0.45) solar, and 3.78 (3.58–3.98) $\times 10^{20}$ cm^{-2}. The derived temperatures are significantly lower than that obtained from the GIS data for the corresponding central region. This temperature discrepancy between the GIS and the PSPC spectra indicates that the emission consists of multiple temperatures. This is not surprising, because, even if the central cluster region is filled with cool plasma, there must be an inevitable contribution from the foreground and background regions of the cluster where the temperature is ~ 3.4 keV.

As a next step, we performed simultaneous fitting of the PSPC and GIS spectra. Because of the broad XRT PSF, the derived GIS spectrum within 1'.5 radius consists of X-ray flux not only from the corresponding sky region but also from outer regions of the sky. However, the contamination from outside the 0'–1'.5 sky region does not significantly affect the results. This is clear from the fact that the annular spectral analysis performed in § 3 and the simultaneous fitting of the five GIS spectra in § 6.1 gave the same results for the central 1'.5 region. Therefore, we used only the central 0'–1'.5 GIS spectrum for the joint analysis with the PSPC spectrum. The effective area for the GIS spectrum was calculated from the PSPC image within 1'.5 convolved with the GIS+XRT PSFs. That effective area represents the contribution from the central 1'.5 sky region to the 1'.5 radius detector region.

We found that the single-temperature model cannot explain the PSPC and GIS spectrum simultaneously. A single-temperature RS model and MEKA model gave minimum χ^2 values of 89.9 and 92.4, respectively, for 60 dof. There must be at least two different temperature components. We attempted the following two types of models to fit the PSPC and GIS spectra simultaneously. Model 1 is a two-temperature model, that is, two different temperature components coexist within 1'.5. The fitting parameters are the two temperatures, their emission measures, common abundances, and the Galactic absorption. We allow the emission measures of the hot component for the PSPC and

GIS spectra to vary independently, but constrain all other parameters to be equal. We employed the RS model and the MEKA model as the plasma emission code. We derived acceptable fits in both cases. The best-fit model is shown in Figure 11, and the derived parameters are summarized in Table 4. The fraction of the cool component, the cool component percentage in the emission measure (EM), defined as $F_{cool} \equiv EM(T_{cool})/EM(r < 1'.5)$, was $\sim 2\%$. Figure 12a shows the χ^2 contours in the F_{cool}-T_{cool} space.

Model 2 is a projected cooling flow model which is expressed as CF($\dot{M}$, T_{max}, T_{min}) + P(T_{max}), where CF is the cooling flow model of Mushotzky & Szymkowiak (1988), and P represents the additional isothermal component. CF is a function of the mass deposition rate $\dot{M}$, the maximum temperature T_{max} from which the gas cools, and the minimum temperature T_{min} to which the gas cools. The temperature is distributed continuously from T_{max} to T_{min}, and each temperature component has emission measure which is inversely proportional to the total emissivity of that temperature. The additional isothermal component must have the same temperature as T_{max}. In this model 2, we also applied two different emission codes, the RS model and the MEKA model (the CFLOW and MKCFLOW XSPEC models, respectively, for the CF component) and derived acceptable fits (Table 5). The χ^2 contour map for $\dot{M}$ versus T_{max} is shown in Figure 12b. The estimated mass deposition rate is 60 ± 30 $M_\odot$ yr^{-1}, while the ratio of the cooling flow component to the total emission measure within the 1'.5 region [$F_{CF} \equiv EM(CF)/EM(r < 1'.5)$] was $\sim 8\%$. With both models 1 and 2, the obtained X-ray luminosity within the 1'.5 region was 2.6×10^{44} ergs s^{-1} in the 0.5–4.5 keV band, and is primarily the emission of the hot noncooled component with a temperature of ~ 3.5 keV. The 0.5–4.5 keV luminosity of the cool component of model 1 and the cooling flow component of model 2 are 6.4×10^{42} and 2.8×10^{43} ergs s^{-1}, respectively. The fraction of the hot component is thus far larger than could be explained in terms of the projected foreground/background emission from the off-center regions.

7. SUMMARY AND DISCUSSION

The energy-dependent flux-mixing effect due to the XRT PSF makes it quite difficult to analyze the data of extended sources observed with *ASCA*. In order to perform simultaneous fitting of the X-ray images and spectra, we have calibrated the XRT PSF using the data from Cyg X-1, and have fully taken it into account in the data analysis.

The X-ray radial brightness profile obtained by the *ROSAT* PSPC exhibits a central excess above a single β model within $\sim 1'.5$, as does the radial profile from the *Einstein* IPC data. With *ASCA*, we observed the X-ray surface brightness in higher energy bands up to ~ 10 keV for the first time. Using the newly developed analysis technique, we fitted the radial brightness profiles and found that there is no clear difference among the profiles in different energy bands. This suggests that the central excess emission found

in the soft X-ray images from *Einstein* and *ROSAT* also exists in the higher energy band of 4–10 keV. In particular, we successfully reproduced the GIS radial brightness profile as a sum of two β models. The narrower of the two β components, thought to represent the central excess emission, is required not only below 2 keV but also in harder energy bands, up to 10 keV, assuming a double-β profile in all energy bands.

The simultaneous fitting of the five annular spectra taken from the GIS data gave the radial profiles of the temperature and metal abundance (see Fig. 10). The obtained overall temperature structure is consistent with being isothermal; this result is also consistent with the fact that all the radial profiles are very similar. However, the PSPC spectra accumulated from the region within 1.5, where the surface brightness profile begin to deviate from the β model, gives a significantly lower temperature than that obtained from the GIS spectrum. This means that there must be an additional cool component at the cluster center. Therefore, we jointly analyzed the GIS and PSPC data and successfully fitted both spectra simultaneously with the two-temperature model as well as the cooling flow model (Fig. 11). The cooling flow model gives a mass deposition rate of $60 \pm 30 \ M_\odot \ \mathrm{yr}^{-1}$, an order of magnitude smaller than the $600 \ M_\odot \ \mathrm{yr}^{-1}$ estimated from the *Einstein* data by David et al. (1990). If we assumed that all the flux coming from the central 1.5 region originated from cooling flow, we would derive a value consistent with $600 \ M_\odot \ \mathrm{yr}^{-1}$, using the formula $\dot{M} = 2\mu m_p L_X / 5kT$ and the bolometric luminosity within 1.5 of $L_X \sim 4 \times 10^{44}$ ergs s^{-1}. However, as we showed in § 6, the central 1.5 region cannot be entirely cooled. More than 90% of the total emission measure consists of the hot noncooled component with the temperature ~ 3.5 keV. Therefore, the central excess in the X-ray brightness profile can not be formed only by the cool component.

Since the central region representing the excess emission is mostly occupied by the same hot ICM component that permeates the rest of the cluster, we interpret the central excess emission as evidence for gravitational potential structure. The potential structure can be interpreted as consisting of two distinct components: a large-scale cluster component and a central compact component attributed to the cD galaxy. In previous investigations, such a dual potential structure has been suggested (Thomas, Fabian, & Nulsen 1987; Nulsen & Böhringer 1995) or assumed (e.g., Stewart et al. 1984). The first direct observational evidence of the additional potential dimple around NGC 1399 in the Fornax Cluster was found from the *ASCA* observation (Ikebe et al. 1996). In the case of the Hydra A Cluster, there also must be a central potential dimple around the cD galaxy which primarily causes the central excess in the brightness profile.

Thus far, the central excess brightness seen in many clusters has been interpreted mainly as due to the central temperature decrease of gas, thus providing a basis for the cooling flow. However, our results clearly reveal that the central excess brightness is at least partially caused by the dual potential structure around the cD galaxy. Therefore, the cooling flow rate derived from the central excess brightness can be grossly overestimated, as in the case of the Hydra A Cluster, if the dual potential structure is ignored.

The metal abundance distribution is also a very important subject that is strongly related to the cluster evolution scenario. A detailed measurement has become possible for the first time using *ASCA*. In the Hydra A Cluster, we found an indication of a central concentration in the metal abundance distribution (Fig. 10). *ASCA* has clearly detected the central concentration in the heavy-element abundance distributions in the nearest two clusters, Virgo and Centaurus (Matsumoto et al. 1996; Fukazawa et al. 1994). A similar result has also been discovered in the poor cluster AWM 7 (Xu et al. 1996). The central abundance concentration may be caused by a large contribution by metal-enriched ISM of the cD galaxies, which may not have suffered a ram-pressure–stripping process in the cluster evolution (Tamura et al. 1996), because the cD galaxy is sitting in the bottom of the gravitational potential well. We speculate that all the clusters showing central excess emission in the brightness profile have a central concentration of heavy elements.

Based on the results from the simultaneous fitting of the GIS and PSPC spectra with the two-temperature model (model 1 in § 6.2), we calculated the mass of the cool component gas. We assumed that the cool component coexists with the hot component within the 1.5 region, and the local pressure balance is achieved between the cool component and the hot component as $n_{\mathrm{cool}} T_{\mathrm{cool}} = n_{\mathrm{hot}} T_{\mathrm{hot}}$. The mass of the cool component gas is estimated to be $M_{\mathrm{gas}} \sim 6 \times 10^9 \ M_\odot$; and its filling factor, that is, the volume fraction of the cool component, is $\sim 6 \times 10^{-4}$. On the other hand, if the cool component is concentrated at the center, and the pressure equilibrium is achieved at the boundary of the cool component and the hot component, the cool component would be distributed out to ~ 5 kpc and would have a total mass of $M_{\mathrm{gas}} \sim 2 \times 10^9 \ M_\odot$. These values are about 0.1%–0.4% of the stellar mass of the cD galaxy 3C 218 = Hydra A, estimated to be $1.5 \times 10^{12} \ M_\odot$ based on the assumption of $M/L_B = 6(M/L_B)_\odot$ and $\log L_B = 11.4$. This is comparable to that in other non-cD ellipticals (Forman, Jones, & Tucker 1985).

APPENDIX

PSF CALIBRATION

For the analysis of the extended sources, adequate knowledge of the XRT PSF is required. However, neither the calibration experiment performed on the ground nor the ray-tracing code could reproduce the PSFs with sufficient accuracy, and in-orbit calibration was required. As we described in § 4, the PSF has largely extended outskirts and depends on the X-ray energies. In
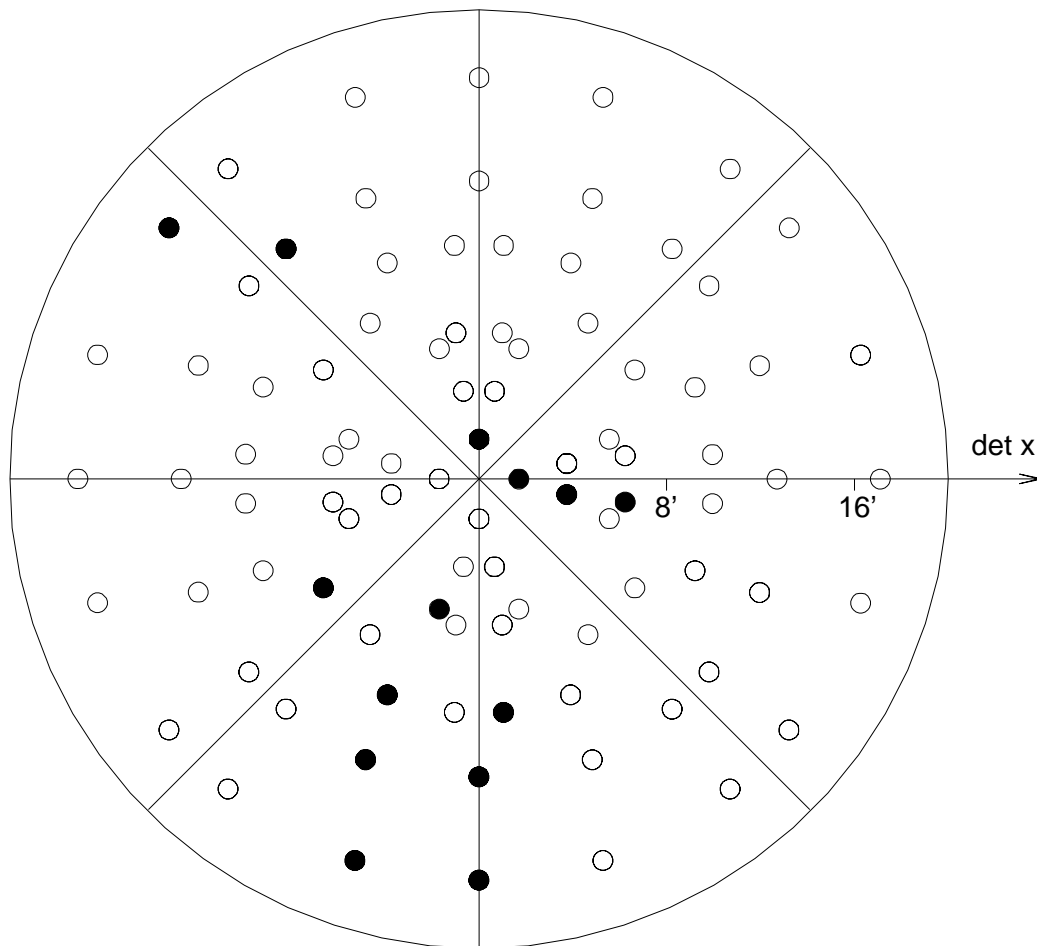
FIG. 13.—Positions on the focal plane where Cyg X-1 is observed (*filled circles*) and the positions that are identical to those assuming symmetry (*open circles*).

addition to these characteristics, we should note the difficulties of the PSF modeling caused by its lack of cylindrical symmetry and strong dependency on the position on the focal plane. Accordingly, we have developed the method of reproducing the PSFs by interpolating among a set of data from Cyg X-1 taken at various positions on the focal plane (Takahashi et al. 1995; Ikebe 1995). Cyg X-1 was selected because it is one of the brightest point X-ray sources with a hard spectrum. With this method we can only reproduce the XRT + GIS PSFs. Because any point source bright enough to yield a sufficient number of signal photons within realistic observing times would cause considerable event pileup in the SIS data, the XRT + SIS PSFs is difficult to obtain.

The observations of Cyg X-1 used to produce the XRT + GIS PSFs were performed in 1993 November, 1994 November, and 1995 May. Taking advantage of the 5' relative misalignment between the two XRTs equipped the two GIS sensors, GIS-S2 and GIS-S3, we obtained 14 sample positions on the focal plane with seven pointing observations (Fig. 13). Assuming that the eight quadrants of the two XRTs are identical and perfectly symmetric, we can have practically 92 PSF data sets. We have divided each pointing data set into eight energy bands, 0.5–1 keV, 1–2 keV, 2–3 keV, 3–4 keV, 4–5 keV, 5–6 keV, 6–8 keV, and 8–12 keV, yielding a PSF image database composed of 8×92 PSF images. When we produce a PSF at a given position and energy, we select the nearest two to eight sample positions in Figure 13 and the nearest two energy bands, and linearly interpolate them in the position and energy space.

We examined the accuracy of the generated PSFs by comparing the synthesized PSF with the observed data of 3C 273, in terms of their radial profiles centered on the peak. At the energies above 2 keV, the radial profiles agree reasonably. On the other hand, below the 2 keV band, the PSFs generated from Cyg X-1 data have larger HPDs by $\sim 0\rlap{.}'2$ and are significantly wider than those of 3C 273. This may be caused by the intrinsic extension in the X-ray emission from Cyg X-1 due to the X-ray scattering by interstellar dust grains (Mitsuda et al. 1990). Therefore, we improved the PSFs below 2 keV as follows. For the 1–2 keV band PSF images in the database, we combined the outskirts region ($r > 6'$) of the 1–2 keV band with the core ($r < 6'$) of the 2–3 keV band images convolved with a Gaussian of $\sigma = 0\rlap{.}'125$. As the 0.5–1 keV band images, we used the 2–3 keV band images which is smoothed with a Gaussian of $\sigma = 0\rlap{.}'625$.

Figure 14 shows the comparison of the PSFs thus obtained with those of the data from 3C 273, in terms of their radial profiles centered on the peak. Based on studies using Monte Carlo simulation, we introduced a systematic error of 5% for the model predictions in the analysis in this paper. The systematic error of the produced PSFs may be caused by the inaccuracy of the assumption that the eight quadrants of the two XRTs are identical and symmetric. Further, additional observation of Cyg X-1 would reduce the systematic error in the interpolation procedure on the focal plane.
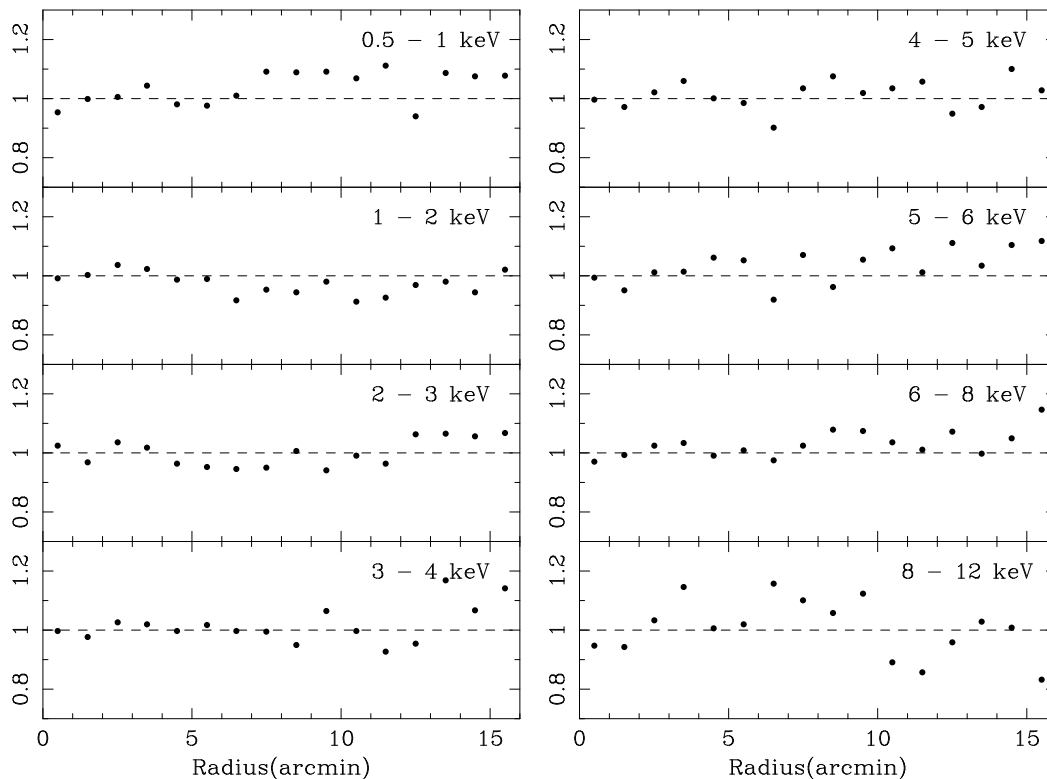
FIG. 14.—Comparison of the radial brightness profiles of the 3C 273 data with those of the PSFs that we used in our analysis. The PSFs are reproduced by interpolating among the actual observed data of Cyg X-1 or their modified images (see text). The vertical axis shows the radial profile ratios (data/PSF) averaged over eight data sets of 3C 237.

REFERENCES

Anders, E., & Grevesse, N. 1989. Geochim. Cosmochim. Acta, 53, 197
Canizares, C. R., et al. 1979, ApJ, 234, L33
Churazov, E., Gilfanov, M., Forman, W., & Jones, C. 1996, ApJ, 471, 673
David, L. P., Arnaud, K., Forman, W., & Jones, C. 1990, ApJ, 356, 32
Day, C., Arnaud, K., Ebisawa, K., Gotthelf, E., Ingham, J., Mukai, K., & White, N. 1995, The ABC Guide to ASCA Data Reduction, Version 4, ASCA Guest Observer Facility, NASA/Goddard Space Flight Center
Edge, A. C., Stewart, G. C., & Fabian, A. C. 1992, MNRAS, 258, 177
Ekers, R. D., & Simkin, S. M. 1983, ApJ, 265, 85
Fabian, A. C. 1994, ARA&A, 32, 277
Forman, W., Jones, C., & Tucker, W. 1985, ApJ, 293, 102
Fukazawa, Y. 1996, private communication
Fukazawa, Y., Ohashi, T., Fabian, A. C., Canizares, C. R., Ikebe, Y., Makishima, K., Mushotzky, R. F., & Yamashita, K. 1994, PASJ, 46, L55
Henriksen, M. J., & Markevitch, M. L. 1996, ApJ, 466, L79
Honda, H., et al. 1996, ApJ, 473, L71
Ikebe, Y. 1995, Ph.D. thesis, Univ. Tokyo
Ikebe, Y., et al. 1994, in Proc. 29th Rencontre de Moriond, 14th Moriond Astrophysics Meetings, Clusters of Galaxies, ed. F. Durret, A. Mazure, & J. Trân Thanh Vân (Gif-sur-Yvette: Editions Frontières), 163
———. 1996, Nature, 379, 427
Kaastra, J. S. 1992, An X-Ray Spectral Code for Optically Thin Plasmas (Internal SRON-Leiden Rep., updated version 2.0)
Kato, T., Tabara, H., Inoue, M, & Aizu, K. 1987, Nature, 329, 223
Kikuchi, K., Ohashi, T., Yamasaki, N., Ikebe, Y., Ishisaki, Y., Fukazawa, Y., Takahashi, T., & Sarazin, C. L. 1995, in Frontiers Science Ser., No. 15, UV and X-Ray Spectroscopy of Astrophysical and Laboratory Plasmas, ed. K. Yamashita & T. Watanabe (Tokyo: Universal Academy Press), 391
Kriss, G. A., Cioffi. D. F., & Canizares, C. R. 1983, ApJ, 272, 439
Makishima, K., et al. 1996, PASJ, 48, 171
Markevitch, M. 1996, ApJ, 465, L1
Markevitch, M., Mushotzky, R., Inoue, H., Yamashita, K., Furuzawa, A., & Tawara, Y. 1996a, ApJ, 456, 437
Markevitch, M., Sarazin, C. L., & Irwin, J. A. 1996b, ApJ, 472, L17
Markevitch, M., & Vikhlinin, A. 1997, ApJ, 474, 84
Matsumoto, H., Koyama, K., Awaki, H., Tomida, H., Tsuru, T., Mushotzky, R., & Hatsukade, I. 1996, PASJ, 48, 201
Matsuzawa, H., Matsuoka, M., Ikebe, Y., Mihara, T., & Yamashita, K. 1996, PASJ, 48, 565
Mewe, R., Gronenschild, E. H. B. M., & van den Oord, G. H. J. 1985, A&AS, 62, 197

Mewe, R., Lemen, J. R., & van den Oord, G. H. J. 1986, A&AS, 65, 511
Mitsuda, K., Takeshima, T., Kii, T., & Kawai, N. 1990, ApJ, 353, 480
Mushotzky, R., Loewenstein, M., Arnaud, K. A., Tamura, T., Fukazawa, Y., Matsushita, K., Kikuchi, K., & Hatsukade, I. 1996, ApJ, 466, 686
Mushotzky, R. F., & Szymkowiak, A. E. 1988, in Cooling Flows in Clusters and Galaxies, ed. A. C. Fabian (Dordrecht: Kluwer), 53
Nulsen, P. E. J., & Böhringer, H. 1995, A&A, 301, 865
Ohashi, T., et al. 1994, in Frontiers Science Ser., No.12, New Horizon of X-Ray Astronomy: First Results from ASCA, ed. F. Makino & T. Ohashi (Tokyo: Universal Academy Press), 273
———. 1995, in Frontiers Science Ser., No.15, UV and X-Ray Spectroscopy of Astrophysical and Laboratory Plasmas, ed. K. Yamashita & T. Watanabe (Tokyo: Universal Academy Press), 151
———. 1996, PASJ, 48, 157
Plucinsky, P. P., Snowden, S. L., Briel, U. G., Hasinger, G., & Pfeffermann, E. 1993, ApJ, 418, 519
Raymond, J. C., & Smith, B. W. 1977, ApJS, 35, 419 (RS)
Serlemitsos, P. J., et al. 1995. PASJ, 47, 105
Snowden, S. L. 1995, in WWW home page of ROSAT Guest Observer Facility in NASA/Goddard Space Flight Center, Cookbook for Analysis Procedures for ROSAT XRT/PSPC Observations of Extended Objects and the Diffuse Background
Snowden, S. L., McCammon, D., Burrows, D. N., & Mendenhall, J. A. 1994, ApJ, 424, 714
Snowden, S. L., Plucinsky, P. P., Briel, U., Hasinger, G., & Pfeffermann, E. 1992, ApJ, 393, 819
Stewart, G. C., Fabian, A. C., Jones, C. & Forman, W. 1984, ApJ, 285, 1
Takahashi, T., Markevitch, M., Fukazawa, Y., Ikebe, Y., Ishisaki, Y., Kikuchi, K., Makishima, K., & Tawara, Y. 1995, in ASCA News, No.3, ed. ASCA Guest Observer Facility at NASA/Goddard Space Flight Center, 34
Tamura, T., et al. 1996, PASJ, 48, 671
Tanaka, Y., Inoue, H., & Holt, S. S. 1994, PASJ, 46, L37
Taylor, G. B., Perley, R. A., Inoue, M., Kato, T., Tabara, H., & Aizu, K. 1990, ApJ, 360, 41
Thomas, P., Fabian, A. C., & Nulsen, P. E. 1987, MNRAS, 228, 973
Tsuru, T. 1991, Ph.D. thesis, Univ. Tokyo
Xu, H., Ezawa, H., Fukazawa, Y., Kikuchi, K., Makishima, K., Ohashi, T., & Tamuda, T. 1996, PASJ, in press